

TUNL REU I  
RESEARCH REPORT

26 MAY 2015 – 1 AUGUST 2015

TRIANGLE UNIVERSITIES NUCLEAR LABORATORY

DUKE UNIVERSITY  
NORTH CAROLINA STATE UNIVERSITY  
UNIVERSITY OF NORTH CAROLINA AT CHAPEL HILL  
Box 90308, DURHAM, NORTH CAROLINA 27708-0308, USA

The research described in this report is supported by the United States Department of Energy, Office of Science (Low Energy Nuclear Physics and Medium Energy Nuclear Physics Programs), under:

Grant No. DE-FG02-97ER41033 (Duke University),  
Grant No. DE-FG02-97ER41042 (North Carolina State University), and  
Grant No. DE-FG02-97ER41041 (University of North Carolina).

The TUNL Research Experiences for Undergraduates (REU) Program is supported by the National Science Foundation under:

Grant No. NSF-PHY-1461204.

# Contents

<b>Introduction</b>	<b>iv</b>
<b>Personnel</b>	<b>v</b>
<b>1 Research Based at Duke</b>	<b>1</b>
1.1 The Neutron Capture Cross Section on $^{63,65}\text{Cu}$ Between 0.4 and 7.5 MeV . . . . .	2
1.2 Commissioning the Enge Focal Plane Detector . . . . .	4
1.3 A Brief Exploration of Low-Threshold Detectors . . . . .	6
1.4 Effective Operators for Double-Beta Decay . . . . .	8
1.5 Timing Reconstruction Algorithm for $\gamma$ -Ray Detections . . . . .	10
1.6 Nuclear Data Compilation for Beta Decay Isotopes . . . . .	12
1.7 Visualization of Water-Cherenkov Outer Detectors . . . . .	14
1.8 Estimating Detector Efficiency and Statistical Errors in HALO . . . . .	16
<b>2 Research Based at CERN</b>	<b>18</b>
2.1 Searches for New Force Carriers with the ATLAS Experiment . . . . .	19
2.2 Visualization Studies for Advanced Jet-Tagging Algorithms . . . . .	21
2.3 Upgrades and Development for the Semiconductor Tracker of the ATLAS Detector .	23
2.4 R & D for the ATLAS Semiconductor Tracker Upgrade . . . . .	25

# Introduction

An important national goal is to develop a diverse, internationally competitive, and globally engaged workforce in science and engineering. The Research Experiences for Undergraduates (REU) program is part of the effort to achieve that goal. The REU program at the Triangle Universities Nuclear Laboratory (TUNL) and Duke University provides a ten-week opportunity for undergraduate students to pursue research in the areas of nuclear and particle physics. This allows promising physics majors to broaden their education through participation in research at the frontiers of these exciting scientific fields.

In 2015, twelve students participated in the TUNL REU Program: eight spent the summer working on nuclear physics projects on the Duke campus, while the other four spent four weeks at Duke and six weeks at the European Center for Nuclear Research (CERN) near Geneva, Switzerland, working on particle physics projects. Having the nuclear and particle physics students in the same program facilitated cross-field intellectual exchange and the sharing of resources needed by both groups, while the participation of the Duke high energy physics group in the program gives it an international component.

Through introductory lectures and direct research involvement, the students gain experience and insights in the main stages of scientific research in nuclear and particle physics:

- The development of concepts to probe specific features of nuclear matter, particles and fields;
- The design, construction, testing, and installation of equipment and instrumentation;
- Data acquisition, analysis, and interpretation; and
- The dissemination of research results.

In addition to direct involvement in research projects, the REU program at Duke includes activities that are designed to broaden the students' physics foundation, enhance their research skills, and build confidence. These activities include: (1) regular meetings with the program coordinator, (2) research tutorials and special topic lectures, (3) a science writing tutorial, and (4) a required report and presentation by each student at the end of the program. The research reports written by the students form the main body of this document.

# Personnel

## 2015 TUNL REU Participants

<i>Student</i>	<i>Home Institution</i>	<i>Faculty Advisor(s)</i>	<i>Class</i>
Oz Amram	Carnegie Mellon Univ.	Al Goshaw	Jr
Isabel Bray	Clarkson Univ.	Megha Bhike & Werner Tornow	Jr
David Elofson	Bridgewater State Univ.	Ayana Arce	Jr
Katherine Kowal	Lewis & Clark College	Richard Longland	So
Chloe Lindeman	Haverford College	Ayana Arce & Mark Kruse	So
Kirollos Masood	Univ. of Florida	Phil Barbeau	Jr
Reza (Ray) Niazi	Univ. of Oklahoma	Jon Engel	Jr
Kadeem Nibbs	Vassar College	Reyco Henning	Jr
Susan Olmsted	East Tenn State Univ.	John Kelley	Jr
Nathan Perreau	Univ. of North Carolina	Chris Walter	So
Danielle Riggan	Duke Univ.	Kate Scholberg	Jr
Adryanna Smith	Baylor Univ.	Ayana Arce & Mark Kruse	So

## 2015 TUNL REU Administration

*Principal Investigator:*  
Professor Calvin R. Howell  
Director of TUNL

*Co-Principal Investigator:*  
Professor Ayana Arce

*Program Coordinator:*  
Dr. Alexander Crowell



PARTICIPANTS IN THE TUNL RESEARCH EXPERIENCE FOR UNDERGRADUATES (REU) PROGRAM ARE SHOWN ON THE DUKE CAMPUS. SHOWN IN THE PHOTOGRAPH FROM LEFT TO RIGHT ARE: (FRONT ROW) ADRYANNA SMITH (BAYLOR UNIVERSITY), SUSAN OLMSTED (EAST TENNESSEE STATE UNIVERSITY), KATIE KOWAL (LEWIS AND CLARK COLLEGE), RAY NIAZI (UNIVERSITY OF OKLAHOMA), CHLOE LINDEMAN (HAVERFORD COLLEGE), DANIELE RIGGIN (DUKE UNIVERSITY), ISABEL BRAY (CLARKSON UNIVERSITY); (BACK ROW) KIROLLOS MASOOD (UNIVERSITY OF FLORIDA), OZ AMRAM (CARNEGIE MELLON UNIVERSITY), NATHAN PERREAU (UNIVERSITY OF NORTH CAROLINA AT CHAPEL HILL), KADEEM NIBBS (VASSAR COLLEGE), AND DAVE ELOFSON (BRIDGEWATER STATE UNIVERSITY).

# Research Based at Duke

---

Chapter 1

## 1.1 The Neutron Capture Cross Section on $^{63,65}\text{Cu}$ Between 0.4 and 7.5 MeV

I. BRAY, *REU Student, Clarkson University*; M. BHIKE, KRISHICHAYAN, W. TORNOW, *TUNL*

Copper is being used as a cooling and shielding material in most searches for neutrinoless double-beta decay. In order to accurately interpret background events in such searches, the cross sections of neutron-induced reactions on copper must be known. We have measured the cross section of the  $^{63,65}\text{Cu}(n,\gamma)^{64,66}\text{Cu}$  reactions using target activation at energies from 0.4 MeV to 7.5 MeV. Previous data were limited to energies below 3 MeV. Our results are compared to predictions from two nuclear data libraries.

Sophisticated experiments around the world are seeking to observe neutrinoless double-beta decay ( $0\nu\beta\beta$ ). Two such collaborations are GERDA, at the Gran Sasso Laboratory in Italy, and EXO-200, at the Waste Isolation Pilot Plant in New Mexico [Tor14]. These experiments utilize different candidates for  $0\nu\beta\beta$  decay— $^{76}\text{Ge}$  ( $Q = 2039$  keV) and  $^{136}\text{Xe}$  ( $Q = 2457.8$  keV), respectively—but both rely on copper as a shielding and cooling material [Tor14]. The reduction of natural background is absolutely imperative in order to detect the signal from  $0\nu\beta\beta$  decay. Therefore extensive knowledge of the sources of background in the experimental setups is needed, and both GERDA and EXO are vulnerable to background from neutron-induced reactions on copper. Current data on neutron capture on  $^{63,65}\text{Cu}$  exists for neutron energies up to 3 MeV, with sparse data at higher energies. The goal of this experiment is to measure the cross section for neutron capture on these copper isotopes to aid in the reduction of background signals in  $0\nu\beta\beta$ -decay searches.

The experiment was performed at TUNL via the neutron activation method [Bhi14]. The targets were copper disks 1.9 cm in diameter. The thicknesses of the  $^{63}\text{Cu}$  targets varied between 1 and 1.25 mm, while the thickness of the  $^{65}\text{Cu}$  target was 2.5 mm. To monitor the neutron flux, indium foils of the same area were attached to the front and back sides of the target. The target and monitor foils were surrounded by a cadmium cage to reduce the effect of thermal neutrons. Monoenergetic neutrons were produced at various energies through using two reactions. The  $^3\text{H}(p,n)^3\text{He}$  reaction was employed to produce neutron beams at six different energies between

0.4 and 4 MeV. The  $^2\text{H}(d,n)^3\text{He}$  reaction was utilized for four energies between 4 and 8 MeV. As shown in Fig. 1.1, the experimental setup for the measurements with  $^2\text{H}(d,n)^3\text{He}$  consists of a 3 cm long gas cell pressurized to 4 atm with high-purity deuterium gas. A 6.5 mm Havar foil separates the gas from the accelerator vacuum. A liquid-scintillator-based neutron detector positioned at  $0^\circ$  relative to the incident proton or deuteron beam direction at a distance of about 3 m from the neutron production target was used to monitor the neutron flux.

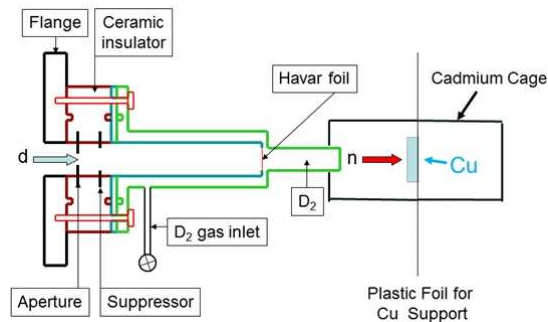


**Figure 1.1:** Schematic view of the experimental arrangement for the  $^{63,65}\text{Cu}(n,\gamma)^{64,66}\text{Cu}$  cross-section measurements using the  $^2\text{H}(d,n)^3\text{He}$  reaction.

After irradiation, off-line  $\gamma$ -ray spectroscopy was employed to count the induced activity in the targets using well-shielded and calibrated high-purity germanium (HPGe) detectors of 60% relative efficiency. Table 1.1 gives the properties of the  $\gamma$ -ray transitions we used.

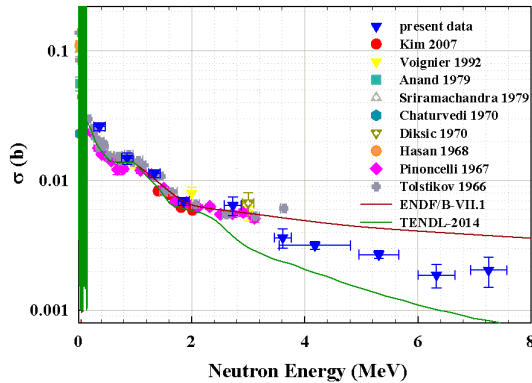
Due to the 5.12 min half-life of  $^{66}\text{Cu}$ , a quick transfer from irradiation to measurement was necessary. Therefore, an HPGe detector

**Table 1.1: Properties of the  $\gamma$ -ray transitions used for the  $^{63,65}\text{Cu}(n,\gamma)^{64,66}\text{Cu}$  reactions and the indium monitor reactions**

Nucleus	$T_{1/2}$	$E_\gamma$ (keV)	$I_\gamma$ (%)
$^{63}\text{Cu}(n,\gamma)^{64}\text{Cu}$	12.701(2) h	511.0	35.2
$^{65}\text{Cu}(n,\gamma)^{66}\text{Cu}$	5.120(14) m	1039.2	9.23
$^{115}\text{In}(n,n')^{115m}\text{In}$	4.486(4) h	336.24	45.8
$^{115}\text{In}(n,\gamma)^{116m1}\text{In}$	54.29(17) m	1293.56	84.8

and its data-acquisition system were mounted in the hallway directly outside the target room at TUNL. This system reduced transfer time to between 30 and 90 seconds and was used for all measurements of the  $^{65}\text{Cu}(n,\gamma)^{66}\text{Cu}$  except at 4.5 MeV. All other measurements were taken in TUNL's low-background counting facility.

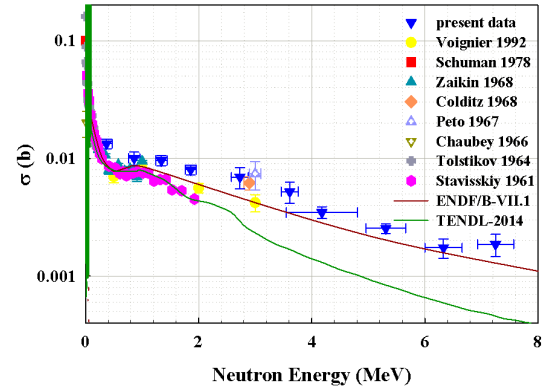
As has been described in Ref. [Bhi14], auxiliary measurements were performed with an untritiated "neutron production" target at neutron energies of 2.73 MeV and 3.61 MeV to account for so-called off-energy neutrons. Auxiliary measurements were also done at the energies of 6.33 MeV and 7.5 MeV with an empty deuterium cell to correct for off-energy neutrons.

**Figure 1.2: Comparison plot of the cross-section data for  $^{63}\text{Cu}(n,\gamma)^{64}\text{Cu}$  with existing data and the evaluations ENDF/B-VII.1 and TENDL-2014.**

Our results for the  $^{63}\text{Cu}(n,\gamma)^{64}\text{Cu}$  reaction are plotted in Fig. 1.2. The cross-section values are in the range of 30 to 1 mb for incident neutrons of 0.4 to 7.5 MeV. Our data agree well with the existing data from 0.37 to 2.73 MeV. From 3.6 to 7.5 MeV they are close to an average of the two evaluations shown, ENDF/B-VII.1 and TENDL-2014.

Our results for the  $^{65}\text{Cu}(n,\gamma)^{66}\text{Cu}$  reaction are plotted in Fig. 1.3. The data from this work

are slightly higher than the existing data between 0.37 and 3.6 MeV, but agree well with the evaluation ENDF/B-VII.1 from 4.5 to 7.5 MeV. TENDL-2014 predicts lower values than the present data. It is worth noting that much of the existing data in the low-energy region are relatively old. Those experiments were performed with NaI scintillator detectors, whereas the present work used high-resolution HPGe detectors.

**Figure 1.3: Comparison plot of the cross-section data for  $^{65}\text{Cu}(n,\gamma)^{66}\text{Cu}$  with existing data and the evaluations ENDF/B-VII.1 and TENDL-2014.**

The present work provides the first neutron capture cross-section data on  $^{63,65}\text{Cu}$  in the incident neutron energy range from 4 to 8 MeV and supplements existing data from 0.4 to 4 MeV. The data are important to improve evaluations such as ENDF/B-VII.1 and TENDL-2014 and to provide valuable knowledge of potential sources of background radiation in the ongoing searches for neutrinoless double-beta decay.

[Bhi14] M. Bhike and W. Tornow, Phys. Rev. C, **89**, , 031602(R) (2014).

[Tor14] W. Tornow, (2014), arXiv:1412.0734v1 [nucl-ex].

## 1.2 Commissioning the Enge Focal Plane Detector

K.M. KOWAL, C.A. MARSHALL, R.L. LONGLAND, *TUNL*

The Enge Split-Pole Magnetic Spectrometer is used to measure the energy of charged particles in nuclear reactions by recording their positions in a focal plane detector. We constructed the detector, improved its vacuum system, and integrated the detector's signals with a data acquisition system. Position measurements were recorded using a collimated  $^{241}\text{Am}$  source. Further development is required to improve the stability and performance of the detector.

The precise measurement of nuclear reactions provides the foundation for nuclear astrophysics and the predictions of stellar models, where key reactions provide constraints on nucleosynthesis and energy production in stars [Wie12]. The building blocks for understanding these reactions are nuclear cross sections, and particle spectroscopy makes it possible to determine them, particularly when direct laboratory measurements are not feasible.

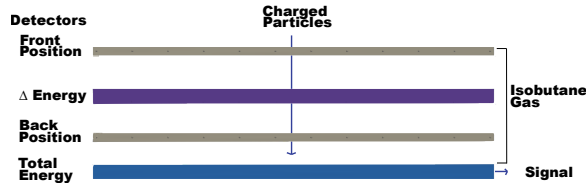


Figure 1.4: The focal plane detector is comprised of four separate detectors, enabling it to identify particles and capture their spread in position

The energy of charged particles exiting nuclear reactions can be precisely measured using the Enge split-pole spectrometer [Spe67], which bends charged particles through a magnetic field. Their orbital radii can then be related to their initial energy. The energy resolution of the split-pole spectrograph is limited by energy straggling in the target and the resolution of the detection system placed at the focal plane. Energy straggling in the target typically amounts to less than 10 parts per million, so the challenge arises in designing a detector capable of the same resolution as the Enge. The focal plane detector was developed to achieve this goal [Hal99]. It also allows us to determine particle type, energy, and trajectory.

The focal plane detector, shown in Fig. 1.4, is

comprised of four main elements: front and back position sensors, separated by an energy loss section and followed by a total energy section. The position and energy loss sections are filled with isobutane gas, which is easy to ionize and relatively noncorrosive to the inside of the detector.

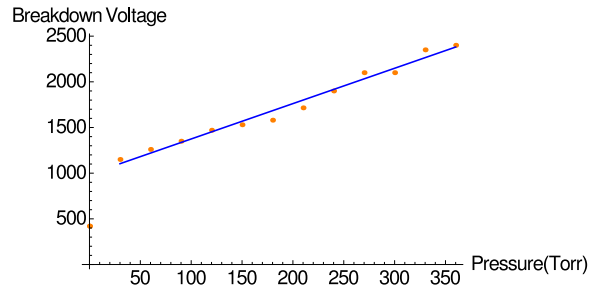


Figure 1.5: Breakdown voltage in the position section's high voltage wires as a function of detector pressure.

From the two position detectors, we capture the location and trajectory of the charged particles. Signals generated in the position sections travel to both ends of a delay line, resulting in a time difference in signal arrival times that depends on the position an event occurred. Using a time-to-amplitude converter, we reconstruct the time difference between the two signals in the front detector and identify where the particle entered the detector. From the additional use of the back position detector, we measure the angle at which the particle travels. This allows us to correct for aberrations in the focal plane and imprecise positioning of the detector. By capturing the particles' trajectories, the detector enables us to ray-trace this plane in the computer after the data measurement and thus obtain higher energy resolution.

The energy loss detector uses a proportional counter. Its purpose is to aid in particle identification. In some cases, two charged particle species entering the detector can carry the same total energy, but, as is the case with an alpha particle and a proton, they differ in their rate of energy loss in the proportional counter. This enables us to separate the events for the particle type of interest.

In the final section a scintillator stops the particles and measures their total energy. Our design incorporates aluminum foil surrounding the scintillator. The foil serves both to protect the detector from external light and to internally reflect the emitted photons created by the incoming charged particles.

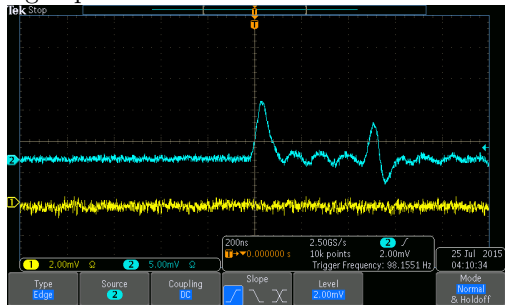


Figure 1.6: Front left position signal. The existence of multiple peaks is problematic.

One challenge in operating this detector is that it is pressurized equipment placed inside a vacuum chamber. O-rings are used between sections to create a vacuum seal. To prevent the cracking or breaking of the o-rings due to overstretching, custom o-rings were spliced and their joints sanded down. A combination of sand paper and Baretex was used to ensure a smooth sealing surface on the aluminum pieces where the o-rings sit. In addition, any wrinkles in the aluminum foil surrounding the scintillator in the total energy detector pose the potential for vacuum leaks. Liberal application of vacuum grease was found to lessen their impact. Imprecise machining of the feed-through fittings was also repaired using Torr seal. Ultimately, our largest problem was that the machined o-ring grooves in our metal pieces were too deep. Replacements are being constructed.

Another concern with this detector is sparking. Any crease in the aluminized mylar foil used as a ground plane in both the position and energy loss sections can result in a spark. To maximize signal quality, 2000 V must be applied to the an-

ode wires in our position sections. We were able to apply up to 1500 V sporadically before sparking occurred. This could indicate either dust or a fray in one of the wires. Figure 1.5 shows a potential correlation between the pressure inside the detector and the voltage we were able to reach before sparking occurred. However, these data were taken over a couple of hours, and time may have influenced the detector's performance.

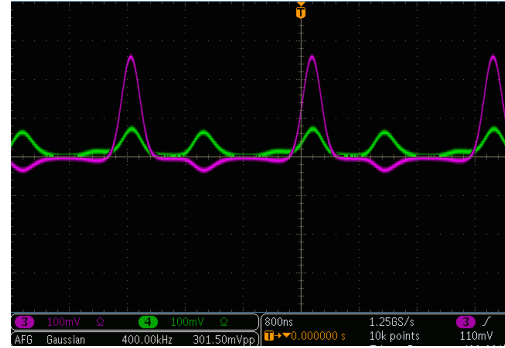


Figure 1.7: Top panel: ungrounded delay line test with the signal (green) and signal generator (purple). Bottom panel: grounded delay test.

Despite these challenges, we were able to collect signals from the position sensitive sections. However, as Fig. 1.6 demonstrates, the signal has two positive peaks instead of the single peak expected. The larger peak on the left will be referred to as the prompt peak. The delay peak is also followed by a negative signal. To investigate the cause of these additional signals, we tested the delay line using a signal generator and found a grounding issue. Figure 1.7 shows that the negative signal as well as the prompt signal disappear when the apparatus is properly grounded.

Future work on this detector will focus on the sparking issues we have found. While we have managed to create vacuum in this device to an acceptable level for obtaining valid signals, sparking will be the next challenge to overcome.

- 
- [Hal99] S. E. Hale, Jr., Ph.D. thesis, The University of North Carolina at Chapel Hill, 1999.
- [Spe67] J. E. Spencer and H. A. Enge, *Nucl. Instrum. Methods*, **49**, 181 (1967).
- [Wie12] M. Wiescher, F. Käppeler, and K. Langanke, *Ann. Rev. Astro. Astrophys.*, **50**, 165 (2012).

### 1.3 A Brief Exploration of Low-Threshold Detectors

K. MASOOD, P.S. BARBEAU, G. RICH, *TUNL*

We are developing prototype low-noise, low-threshold, gas-filled detectors for use in modern particle-physics research and for exploring the use of alkane targets for reactor anti-neutrino experiments involving observation of inverse beta decay. We have successfully operated a prototype chamber using both isobutane and P-10 at pressures between 1 and 30 psi. A threshold of 150 eV is demonstrated with only preliminary noise- and threshold-reduction efforts. With very modest shielding, background count rates are below  $1000 \text{ counts keV}^{-1} \text{ kg}^{-1} \text{ day}^{-1}$ .

Low-threshold gas-filled detectors are a powerful tool in a variety of possible applications, including inverse beta-decay detection; exotic efforts such as direct-detection spin-dependent WIMP searches; and observations of never-before-observed interactions predicted by the standard model, such as coherent, elastic neutrino-nucleus scattering ( $\text{CE}\nu\text{NS}$ ) [Col01]. Considering the usual scale and investment involved in such projects, success in just one of these goals would be a considerable innovation. With this in mind, the goal this summer was to develop and characterize prototype detectors with such experiments in mind.



Figure 1.8: An exterior view of our first prototype.

The initial design was a proportional counter with a roughly cylindrical geometry. A gold-tungsten anode wire was strung down the center of a series of Conflat flanges. The design allowed for a high voltage (for our interests, positive) to be applied on the wire, with the outer casing serving as ground. Gas was permitted to flow through two Conflat to Swagelok fittings. Figure 1.8 is a photograph of the detector. The  $^{55}\text{Fe}$  source, when used, was secured to the back of a Conflat blank, as demonstrated in Fig. 1.9.

The detector was then connected to an Ortec 142 preamplifier, an Ortec 672 spectroscopic amplifier, an ADC, and a computer for data acquisition.

A variety of operating voltages and pressures were tested, with the goal of keeping at least one known peak in range for calibration. In addition, layers of aluminum, a copper collimator, and sometimes both, were used to reduce the count rate to prevent signal pile-up. The spectrum taken for each set of conditions had a run time of one hour, except in the cases where the collimator was used, due to the severely reduced rate.

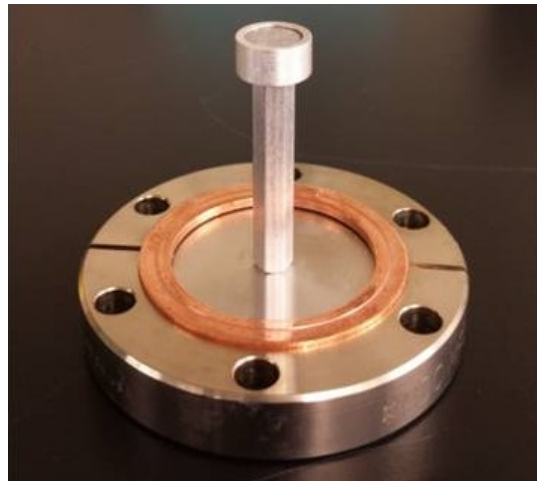
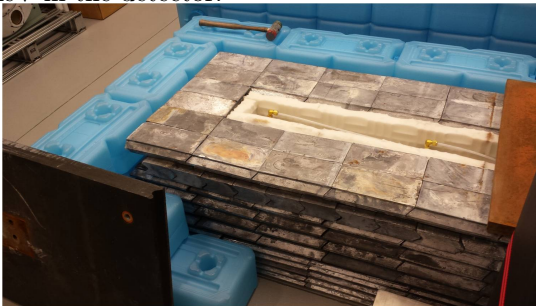


Figure 1.9: A view of the  $^{55}\text{Fe}$  source, mounted on a standoff to be closer to the anode.

Both P-10 (a mixture of 90% argon, 10% methane), and isobutane were used as fill gases, with the operating voltages chosen with consideration of the range on the ADC being used. Then the source was removed and a series of background runs was taken using various amounts of

shielding. Each background run was also taken for an hour. The shielding used is shown in Fig. 1.10.

When using P-10, with pressures of 1 psi, 14 psi, and 30 psi (gauge), adequate voltages were found that display the 5.9 keV X-ray peak associated with the decay of  $^{55}\text{Fe}$ . Also present was a 3 keV peak resulting from a 5.9 keV  $\gamma$  ray ionizing a k-shell electron of Ar and then depositing the remaining energy in the detector. Furthermore, when the aluminum layers were used to reduce the rate, an additional peak was present. It arises when a  $^{55}\text{Fe}$   $\gamma$  ray ionizes a k-shell electron of Al, and an outer-shell electron de-excites to fill this vacancy, depositing the released photon of 1.48 keV in the detector.



**Figure 1.10:** The background reduction methods included a lead castle, water bricks, and borated polyethylene.

An example of a spectrum taken using P-10 is provided in Fig. 1.11. Using the known peaks, a two-point, linear calibration of the x axis can be done. The sizeable peak near threshold is attributed to noise, since it is present in the background run as well. This gives an effective threshold of around 250 eV.

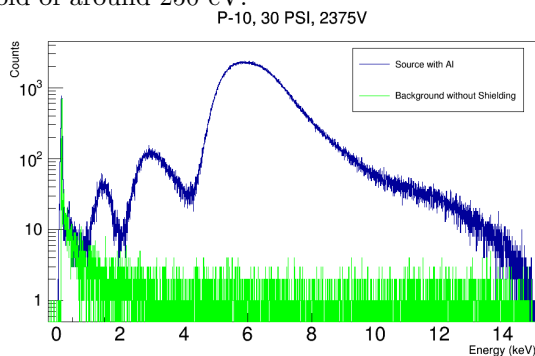


**Figure 1.11:** A sample spectrum taken using P-10 as a fill gas.

Figure 1.12 shows a spectrum taken with isobutane instead. Now, the Ar peak is absent. However, the high energy behavior makes

it harder to perform a calibration, so the axis is set in ADC bins.

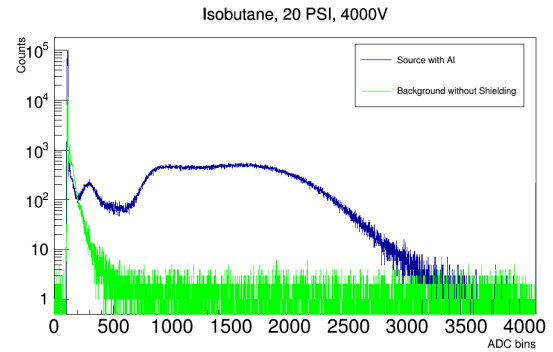


**Figure 1.12:** A sample spectrum taken using isobutane as a fill gas.

Figure 1.13 shows that the background is reduced as more shielding is applied. A rough estimate of the background index so far is  $1000 \text{ counts kg}^{-1} \text{keV}^{-1} \text{day}^{-1}$ .

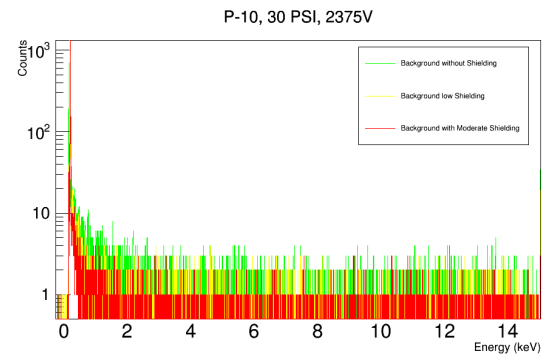


**Figure 1.13:** Spectra of background radiation at various levels of shielding.

While increasing the pressure allows for a greater density, it also reduces the avalanching that occurs. Furthermore, the detector bias cannot be increased arbitrarily in order to lower the threshold, due to the steady loss of energy resolution. A possible improvement would be to change to a point-contact design, which would detect the initial ions rather than relying on avalanching. The use of a CoolFET preamplifier in conjunction with a lower detector capacitance, could very well keep the signal above the noise. In that case, the fill gas could even be liquefied to yield a higher cross section. To further reduce background, muon-veto panels can be placed around the set up to reject unwanted events.

[Col01] J. Collar and Y. Giomataris, Nucl. Instrum. Methods, **471**, 254 (2001).

## 1.4 Effective Operators for Double-Beta Decay

R. NIAZI, *University of Oklahoma, Norman, OK*; J. ENGEL, *University of North Carolina at Chapel Hill, Chapel Hill, NC*

**Neutrinoless double-beta decay is a theoretically predicted process that, if observed, would allow the neutrino mass to be calculated. However, due to a lack of experimentally determined parameters, the calculation of the necessary matrix elements does not have a clear and defined approach. We approximate the infinite shell model space, with that of a 2 shell system and calculate operators and matrix elements.**

To approximate the matrix elements involving the decay operator for neutrinoless double-beta decay, we first must define our system. Since the decay of  $^{76}\text{Ge}$  into  $^{76}\text{Se}$  is a process likely to exhibit neutrinoless double-beta decay, we consider a truncated two-shell system for the nucleons of these species. We only consider systems where all nucleons are paired, so seniority  $\nu$  is equal to 0. Considering a two-particle state within the two-shell system, the goal is to calculate the transition matrix elements of a two-body double-beta decay operator. The first step is to calculate the expectation values of the proton-creation and neutron-destruction operators.

We denote any state of  $Z$  protons and  $N$  neutrons within a  $j$ -shell of a certain  $\Omega = j + 1/2$  as  $|Z N \Omega\rangle$ . After using the quasi-spin operator properties and commutation relations and two applications of the Wigner-Eckart theorem, it can be seen that, for a generalized transition from  $Z$  to  $Z+2$  protons, the expectation value of the proton creation operators is

$$\langle Z+2 0 \Omega | \pi_{j_1 m_1}^\dagger \pi_{j_2 m_2}^\dagger | Z 0 \Omega \rangle = -A_{12} \frac{\sqrt{(Z+2)(2\Omega-Z)}}{2\Omega}, \quad (1.1)$$

where

$$A_{ab} = (-1)^{j_a+m_a} \delta_{j_a, j_b} \delta_{-m_a, m_b} \forall a, b \in \mathbb{N}. \quad (1.2)$$

Likewise, we can find the expectation value of neutron-destruction operators to be

$$\langle 0 N-2 \Omega | \tilde{\nu}_{j_1 m_1} \tilde{\nu}_{j_2 m_2} | 0 N \Omega \rangle = A_{12} \frac{\sqrt{N(2\Omega+2-N)}}{2\Omega}. \quad (1.3)$$

If we define the matrix element of the decay operator for certain total angular momentum values, as  $M_{pqrs} \forall p, q, r, s \in \mathbb{N}$ , such that

$$M_{pqrs} \equiv \langle Z+2 N-2 \Omega | \pi_{j_p m_p}^\dagger \pi_{j_q m_q}^\dagger \tilde{\nu}_{j_r m_r} \tilde{\nu}_{j_s m_s} | Z N \Omega \rangle, \quad (1.4)$$

then one can naturally see that the matrix element of our two-particle, seniority-zero beta-decay operator will be given by

$$M_{1234} = -A_{12} A_{34} \times \frac{\sqrt{(Z+2)(2\Omega-Z)N(2\Omega+2-N)}}{4\Omega^2}. \quad (1.5)$$

With these results in mind, we can find the general form of the decay operator, whose matrix elements we are interested in. Because the decay operator must be a scalar spherical-tensor operator in our formalism, the total system's angular momentum and its projection must be 0. So, the operator of interest,  $\hat{D}$ , will be given by

$$\hat{D} = \sum_{j_1, j_2, j_3, j_4} \sum_J D_{j_1 j_2 j_3 j_4}^J \times \left[ (\pi_{j_1 m_1}^\dagger \pi_{j_2 m_2}^\dagger)^J (\tilde{\nu}_{j_3 m_3} \tilde{\nu}_{j_4 m_4})^J \right]_0^0. \quad (1.6)$$

Now, we can apply the results of Eq. (1.6) to see that the matrix elements of our generalized operator  $D_{ZN} = \langle Z+2 N-2 \Omega | \hat{D} | Z N \Omega \rangle$  will be given by

$$D_{ZN} = - \sum_{j_1, j_3} K D_{j_1 j_1 j_3 j_3}^0 \sqrt{(2j_1 + 1)(2j_3 + 1)}, \quad (1.7)$$

where  $K \equiv \frac{\sqrt{(Z+2)(2\Omega-Z)N(2\Omega+2-N)}}{4\Omega^2}$ . Therefore, all that is needed to determine the matrix elements is to find the constants  $D_{j_1 j_1 j_3 j_3}^0$ .

Having established the form of our decay operator in our two-shell space, we consider the simplest configuration, the one with one pair of nucleons. The Hamiltonian for our two-shell system is given by

$$\hat{H} = \epsilon \hat{N}_2 - G \sum_{a,b=1}^2 (S_{pp}^{\dagger a} S_{pp}^b + S_{nn}^{\dagger a} S_{nn}^b). \quad (1.8)$$

Here  $\epsilon$  is the energy difference between the two shells,  $\hat{N}_2$  is the number operator acting on the second level, and  $G$  is just a constant. The creation operators are given by

$$S_{pp}^{\dagger a} = \frac{1}{2} \sum_{j \in a} \sum_m (-1)^{j-m} \pi_{jm}^{\dagger} \pi_{j-m}^{\dagger}, \quad (1.9)$$

$$S_{nn}^{\dagger a} = \frac{1}{2} \sum_{j \in a} \sum_m (-1)^{j-m} \nu_{jm}^{\dagger} \nu_{j-m}^{\dagger}, \quad (1.10)$$

where  $S_{pp}^a$  and  $S_{nn}^a$  are the adjoints of these terms. We can use what we know about the proton and neutron operators acting upon a state to determine what the operators in the Hamiltonian will do to these states. We can readily see that,

$$S_{pp}^{\dagger a} |Z 0 \Omega_a\rangle = \frac{\sqrt{(Z+2)(2\Omega_a - Z)}}{2} |Z+2 0 \Omega_a\rangle, \quad (1.11)$$

$$S_{pp}^a |Z 0 \Omega_a\rangle = \frac{\sqrt{Z(2\Omega_a + 2 - Z)}}{2} |Z-2 0 \Omega_a\rangle. \quad (1.12)$$

The neutron analogs to these operators have the same form except that  $Z$  would naturally be replaced by  $N$ .

With the results of Eqs. (1.11) and (1.12), we can construct the Hamiltonian for our two-particle state. We only have two possible initial states: one where the neutron pair is in the first level, which is represented as  $|\phi_1\rangle = |0 2 \Omega_1\rangle |0 0 \Omega_2\rangle$ , and one where the neutron pair is in the second level, represented as  $|\phi_2\rangle = |0 0 \Omega_1\rangle |0 2 \Omega_2\rangle$ . This results in a Hamiltonian given in matrix form as

$$\begin{pmatrix} -G\Omega_1 & -G\sqrt{\Omega_1\Omega_2} \\ -G\sqrt{\Omega_1\Omega_2} & 2\epsilon - G\Omega_2 \end{pmatrix}.$$

The simple form of this Hamiltonian allows us diagonalize it easily and find its eigenvalues and eigenvectors. If we define  $O_{1,2} = \Omega_1 + \Omega_2$  and  $O_{1,-2} = \Omega_1 - \Omega_2$ , then the eigenvalues are given by

$$\lambda_{\pm} = \epsilon - \frac{G}{2} O_{1,2\pm} \frac{1}{2} \sqrt{4\epsilon(\epsilon + G O_{1,-2}) + G^2[2\Omega_1\Omega_2 + (\Omega_1^2 + \Omega_2^2)]}. \quad (1.13)$$

Likewise, the eigenvector normalizing factors, denoted by  $a_1$  and  $a_2$ , whose square will be used as the probability amplitudes in the linear combination of the two states  $|\phi_1\rangle$  and  $|\phi_2\rangle$  are given by

$$a_1^2 = \frac{G^2\Omega_1\Omega_2}{(\lambda_- + G\Omega_1)^2 + G^2\Omega_1\Omega_2}, \quad (1.14)$$

$$a_2^2 = \frac{(\lambda_- + G\Omega_1)^2}{(\lambda_- + G\Omega_1)^2 + G^2\Omega_1\Omega_2}. \quad (1.15)$$

For more complicated cases, we have constructed a program that computationally constructs the Hamiltonian and diagonalizes the matrix. This enabled us to construct eigenstates of our truncated 36-nucleon model space that was used to approximate the shells of  $^{76}\text{Ge}$  and  $^{76}\text{Se}$ . With these results in hand, one only has to determine the coefficients of the operator to be able to construct it and to describe the states that it connects. This future work will allow us to determine the full (36 nucleon) and effective (2 nucleon) double-beta decay operators and apply to the entire shell space. The goal would be to determine the disparity of the full and effective operators' matrix elements within the full space. If they are in good agreement—however that may be defined—then one can consider three- and four-body operators, so as to try and increase the coherence of the values. However, if these higher order corrections still cannot remedy a vast disparity in the matrix elements, then this approximation must be reconsidered.

Of course, the Hamiltonian does not take into account neutron-proton coupling and other important interactions. Unfortunately, including these effects would require generators that are not elements of the  $\text{SU}(2)$  algebra. This would make our simplified analytic technique much more complex. Ultimately, there are many more considerations to be taken into account once a final result is achieved, and hopefully there will be a successful method that will allow the neutrino mass to be calculated, if neutrinoless double-beta decay is observed.

## 1.5 Timing Reconstruction Algorithm for $\gamma$ -Ray Detections

K. NIBBS, R. HENNING, C. BARTRAM, G. OTHMAN, *TUNL*

An algorithm has been developed to find the time that scintillation light entered a photomultiplier tube by analyzing the tube's output voltage. The algorithm will hopefully be used to reconstruct ortho-positronium decays and the momentum vectors of the emitted  $\gamma$  rays. An observed angular correlation between the spin axis of the ortho-positronium and the directions of the emitted  $\gamma$  rays will be evidence of CP violation. Though the algorithm has not yet been rigorously tested, it has shown consistency and promise in preliminary trials.

Positronium is a bound state of an electron and a positron. Its triplet state, ortho-positronium or o-Ps, decays into three  $\gamma$  rays. If CP violation occurs in o-Ps decay, it will manifest itself in an angular correlation between the spin axis of the o-Ps and the direction of the three emitted  $\gamma$  rays. The relevant vectors and angles are shown in Fig. 1.14

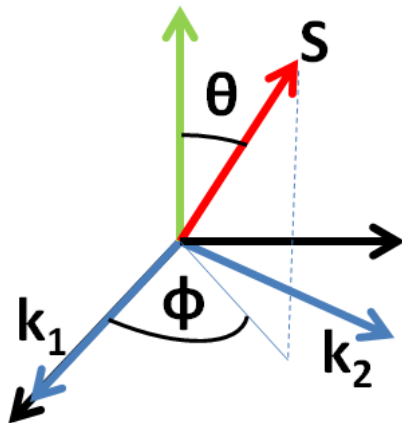


Figure 1.14: Vectors and angles associated with o-Ps decay. The vector  $S$  is the spin axis of the o-Ps,  $k_1$  and  $k_2$  are the momenta of the first and second most energetic  $\gamma$  rays. The green, vertical arrow is the normal to the decay plane.

An asymmetry between positive and negative values of  $2 \cos \theta \cos \phi$ , observed over numerous trials, would suggest such an angular correlation, and therefore CP violation as well. Our APEX detector array is an annular array of sodium iodide (NaI) bars for detecting emitted  $\gamma$  rays. Used in conjunction with our photomultiplier

tubes (PMTs), PMT bases, digitizer, and signal processing techniques, it allows us to calculate and rank their energies as needed.

A more challenging problem, however, has been reconstructing the emitted  $\gamma$  rays' angles of emission. Former graduate student Stephen Daigle found that because of light's attenuation as it moves through a medium, the ratio of the charge amplitudes from the PMTs at opposite ends of the NaI bar gives us the position at which the  $\gamma$  ray struck the bar as shown in Fig. 1.15.

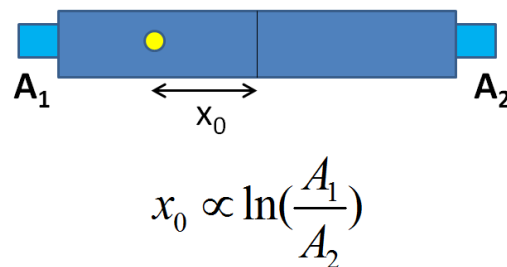


Figure 1.15: Schematic drawing of a NaI test bar and its PMTs.  $A_1$  and  $A_2$  are the charge amplitudes from the first and second PMTs respectively. The yellow circle indicates the event site.

There are, however, a few scenarios where this method will fail. The most readily conceptualized example is an unfortunately placed  $\gamma$ -ray strike at the corner of a NaI bar and against the frame of a PMT. In this scenario, some of the scintillation light will be reflected or absorbed by the PMT, the charge amplitude ratio will be skewed to favor the PMT at the opposite end of the bar, and a faulty position reconstruction will result.

In order to identify, and possibly discard, these problematic o-Ps decays, we devised a second method to complement the first, so that a significant disagreement between the two would indicate an issue. Implementing this method hinged on our ability to identify the time at which light started to enter the PMTs. From the time difference, we would deduce the difference in distances that the light traveled to reach the PMTs and thus, using simple arithmetic, the position in the NaI bar. My main task this summer was to formulate a reliable computer program to determine the  $\gamma$ -ray detection times.

Our team prepared data to test my program by placing a  $^{22}\text{Na}$  source in the center of the APEX array and leaving one NaI bar, along with the signal-processing complex, active. The data were stored in a ROOT file that contained two TTrees, corresponding to the two active PMTs. Each TTree contained numerous waveforms, each containing a digital pulse generated by a  $\gamma$ -ray detection. The waveforms were composed of 4096 digitized voltages sampled at regular time intervals of roughly 10 ns. The waveforms held a steady baseline voltage value in the absence of activity, and then the voltage dropped precipitously when scintillation light entered the PMT before slowly returning to the baseline value. I endeavored to fit the rising edge of the pulse with a linear regression, and then find the best-fit line's intersection with the baseline. The x-coordinate of this intersection would give the time at which light entered the PMT, offset by a constant due to our electronic setup.

To find the pulse in each waveform, I set a reasonable threshold value below the digitizer's

baseline that would rarely be reached without scintillation light being present. I then identified the longest chain of consecutive values below the threshold as the pulse. After finding the pulse's location, I used one function to find the index of the lowest recorded voltage (the peak location), which corresponded to the fastest influx of scintillation light to the PMT, and another function to return the average of the indices between the pulse's peak and its start where the voltage was halfway between the baseline and its peak value (half-peak location). I performed the linear regression fit using all points on the waveform between the pulse's rising half-peak and its start for which the voltage's decrease was linear. The choice to use the early part of the waveform was important, because the waveform was noisier and less linear near the peak location. The x-coordinate of the best-fit line's intersection with the digitizer's baseline was the time at which the scintillation light began entering the PMT.

Although the REU program ended before I could use delay lines to rigorously test the accuracy of my timing-reconstruction algorithm, I found that its calculated detection time consistently fell near the last waveform indices with voltage values at or near the baseline. A few dramatic failures occurred where the x-intersection of the best-fit line and the baseline was outside of the bounds of the waveform. However, upon closer examination, we determined that these resulted from false triggers of the digitizer, which created waveforms without pulses. Future changes, such as selecting different points to perform the linear regression fit, may improve the accuracy of the timing reconstruction.

---

## 1.6 Nuclear Data Compilation for Beta Decay Isotopes

---

S.C. OLMSTED, J.H. KELLEY, G.C. SHEU, *TUNL*

**We have reviewed all available literature to determine the most accurate experimental half-life values for beta-unstable isotopes in the  $A = 3$  to 20 range and found recommended half-life values for most of these isotopes. This analysis will be folded into the Evaluated Nuclear Structure Data File. Meanwhile, our findings have been used to update information given on the TUNL Nuclear Data Evaluation group website.**

The TUNL nuclear data group works with the Nuclear Structure and Decay Data network to compile and evaluate data for use in nuclear physics research and applied technologies. Data evaluation is necessary to deriving meaning from existing data, as well as to establish context for contradicting data. Our project focused on compiling half-life values for use in nuclear research and nuclear physics applications, such as nuclear spectroscopy and the measurement of nuclear reaction cross sections [Bie64]. Therefore, it is important to know half-life values as accurately as possible.

Our goal was to determine half-life values for beta-decay isotopes within the  $A = 3$  to 20 range and to include these values in an online database at TUNL. Ultimately, we hoped to have a central location that contains not just the recommended half lives, but also a list of the compiled articles and raw data that led to that conclusion. Eventually, the results would be transferred to the Evaluated Nuclear Structure Data File (ENSDF) database at the National Nuclear Data Center (NNDC) at Brookhaven National Laboratory.

To accomplish this, we reviewed half-life literature, using the NNDC database to collect an assortment of half-life values for each isotope. The articles were carefully examined to make sure that the half life was actually measured, not compiled from other sources, and that the value was reliable. An example will be given of a case in which a careful literature review was essential.

The data averaging software used was the Visual Averaging Library. We used it to compare eight different averaging techniques: Unweighted Average, Weighted Average, Limitation of Statistical Weights, Normalization Residuals, Rejaval Technique, Method of Best Representation, Bootstrap, and Mandel-Paule. The unweighted average is fairly intuitive: all values are weighed

equally before averaging. However, this method does not make a lot of sense when the values have different uncertainties.

Giving some values more weight based on their relative credibility and accuracy is recommended. Therefore, the weighted average is the preferred method for data evaluation. The weighted average gives the most precise values more weight before averaging. This technique works very well if the data are consistent, as was the case for a little over half of the isotopes we studied.

Sometimes, however, values do not agree as well, and other methods must be used. The next-most-reliable method is the Limitation of Statistical Weights, which manipulates the weights such that no single value carries more than fifty percent of the weight. The reasoning behind this is that, if any one value is that much more precise than the others, then it is possible that the uncertainty has been greatly underestimated, so that the weight should be limited.

The rest of the averaging methods above have similar methods of increasing the values' uncertainties, or otherwise working with the assumption that, if the values have poor agreement, the values must be inaccurate. However, the Weighted Average and the Limitation of Statistical Weights are the most commonly used, since they avoid changing the data to force agreement. Additionally, averaging methods can be compared using a chi-square test.

Note that these methods often produce very low uncertainty values that can be lower than the lowest uncertainty from the individual measurements. Thus we had to be careful to choose the higher uncertainty between the compiled value and the lowest individual one.

As is often the case with data sets, the half-life values sometimes included outliers. The averag-

ing software picks out outliers (values that deviate from the mean) using Chauvenet's Criterion, without taking uncertainties into account. This means that it is as possible for inaccurate values to be targeted, as for the most-reliable ones. Therefore, it was important to take the outliers into account, but to use caution before dismissing anything.

The example of the half-life values of  $^{17}\text{C}$  is shown in Fig. 1.16. This is a fairly intuitive example, in which all of the values agree well. As you can see, the weighted average overlaps with all of the values. As one would expect, the chi-square value of the weighted average is 0.24, much lower than the critical chi-square of 2.37. Therefore, we adopted the weighted average and adjusted the uncertainty to match that of the measurement with the lowest uncertainty.

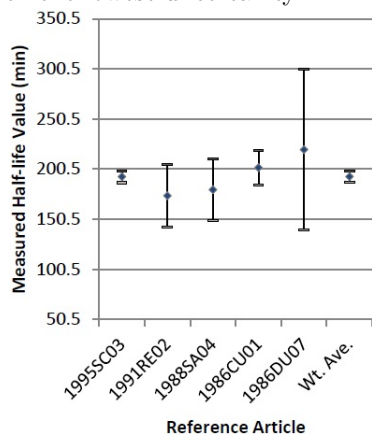


Figure 1.16: Half-life values for  $^{17}\text{C}$  plotted alongside their weighted average.

A very different example is the half-life values of  $^{16}\text{N}$  shown in Fig. 1.17. Here the source articles are arranged chronologically. You can see that these values disagree significantly, the weighted average does not align with many of the values, and the chi-square value is 21.77, compared to a critical chi-square of 1.88.

Before considering different averaging methods, however, it is important to review the articles. Note that the half-life values seem to drop significantly with the fifth article. Upon reviewing this article, we found that, according to Bienlein *et al.*, the first four measurements likely suffered from systematic errors. Bienlein explained that they had found that the background radiation for those measurements was not determined

accurately, causing the researchers to underestimate the background and therefore overestimate the half life [Bie64]. The first four half-life values, then, had to be excluded from the sample. Once the data were recompiled, they agreed nicely, and the new weighted average had a very acceptable chi-square value of 0.48.

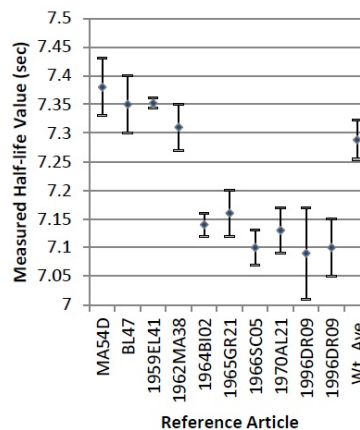


Figure 1.17: Half-life values for  $^{16}\text{N}$  arranged chronologically by year published, plotted alongside their weighted average.

Ultimately, we found half-life values for most of the isotopes. Additionally, we began updating the nuclear-data website at TUNL with recommended half-life values. We also included tables with averaging information for each isotope. These tables list each averaging method, the half-life value produced by the method, either a chi-square value or a percent confidence value (depending on the method), a list of potential outliers, and a recommended value (if a recommended value could be determined). Using these tables, researchers can see the reasoning behind our recommendations.

Future work will include determining half-life values for the isotopes that have poor agreement or outliers. This will require a closer review of the articles, as well as a closer examination of the averaging methods. The averaging method tables that we created will greatly aid in this examination. Additionally, the website will soon be fully activated, and the data will eventually be added to the ENSDF database.

[Bie64] J. Bienlein and E. Kalsch, Nucl. Phys., **50**, 202 (1964).

## 1.7 Visualization of Water-Cherenkov Outer Detectors

N. PERREAU, *University of North Carolina at Chapel Hill, Chapel Hill, NC*; E. O’SULLIVAN, C. WALTER *Duke University, Durham, NC*;

The outer detector for a water-Cherenkov detector determines if a neutrino interaction occurred inside the main detector or externally. Simulations of water-Cherenkov detectors such as Super-Kamiokande and Hyper-Kamiokande have been carried out using the WCSIM software but have not included the outer detector. A new visualizer called RAYTRACER was installed in the simulation code to work alongside the original visualizer and allow the outer detector to be included.

### Background

When neutrinos interact with water, they can emit charged particles that exceed the speed of light in water, producing a cone of light. Water Cherenkov detectors record these neutrino interactions by using photomultiplier tubes (PMTs) to detect the photons from the cone of Cherenkov light. The photons can be used to determine information about the neutrino interaction, including where the interaction occurred, the charged particle emitted, and the speed of the charged particle.

Super-Kamiokande or Super-K is a water-Cherenkov neutrino detector located in the Kamioka Mine in Gifu, Japan. It has 11,000 PMTs, 20 inches in diameter, on the inner detector (ID) to look at the emitted light from neutrino interactions, and 2,000 PMTs, 8 inches in diameter, on the outer detector (OD) that determine when a charged particle is entering from outside the detector. The OD is especially important for rejecting external muons. The water in the OD also prevents external neutrons from entering the ID. Hyper-Kamiokande or Hyper-K is a theoretical upgrade of Super-K that will have ten times the PMTs, and twenty times the volume. The goal of Hyper-K is to measure neutrino interactions with higher statistics, thus opening the way for studies of CP violation of neutrinos, neutrino masses, and cosmic neutrinos.

The software package that simulates water-Cherenkov detectors was written in GEANT4 and is called WCSIM. Currently, WCSIM is primarily being used for the development of the Hyper-K experiment and will have future uses for the Super-K experiment. Configurations in WCSIM

only consisted of the inner portions of Super-K and Hyper-K, and the OD needed to be visualized and designed.

### RAYTRACER Visualizer

The focus of this work was to allow WCSIM to use RAYTRACER and OGLSX as visualizers. OGLSX was already implemented in the code and is used to see results of particle interactions, as shown in Fig. 1.18, but RAYTRACER allows users to visualize the geometry of the detectors more easily. RAYTRACER permits users to view the geometry of the detector from various positions and angles, and to make different detector components invisible.

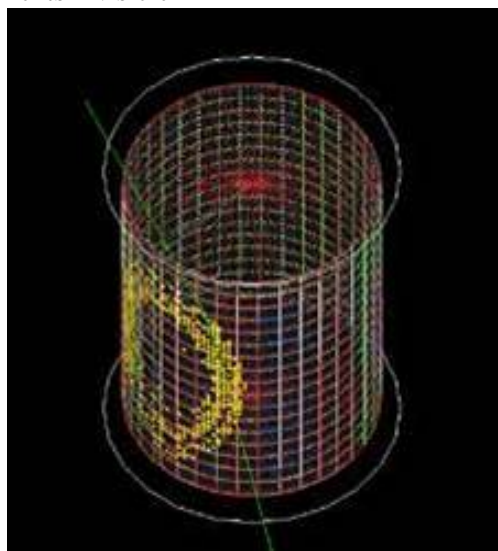
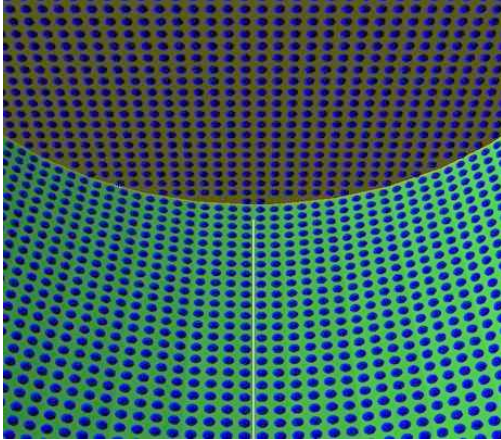


Figure 1.18: Example of OGLSX visualizer output

In GEANT4, structures are created by defin-

ing three volumes: the simple, logical, and physical volumes. They respectively define the shape, attributes, and placement in larger volumes for the structure. The majority of the code implemented to support RAYTRACER consisted of changing visual aspects of logical volumes for the detector volumes. Specifically, the changes were made to control the color and transparency of objects in WCSIM's cylinder and PMT routines.



**Figure 1.19:** RAYTRACER-visualizer output of simulated Super-K design, taken inside the ID looking towards the top corner. PMTs (blue) are shown on the wall (green) and cap (yellow).

In the code for WCSIM, RAYTRACER can now easily be used as a visualizer. A new macro file was created to make changing between OGLSX and RAYTRACER very easy.

### Designing the Outer Detector

With RAYTRACER working in WCSIM, it was relatively simple to include the visualization of the properties of the outer detector (OD). The process started with creating variables for the new PMTs, wall, and caps. These variables include things such as the outer detector radius and the distance between the inner and outer caps. Next, the air and water volumes of WCSIM had to be expanded to include the OD. The final step consisted of placing the PMTs onto the new wall and caps. Examples of RAYTRACER output are shown in Figs. 1.19 and 1.20.

Including the OD in WCSIM was important because the design of Hyper-K needs to be optimized. Visualizing the outer detector and running simulations with it in place can be used to determine this design. WCSIM can now be used to determine the optimal OD properties necessary to tag external muons.

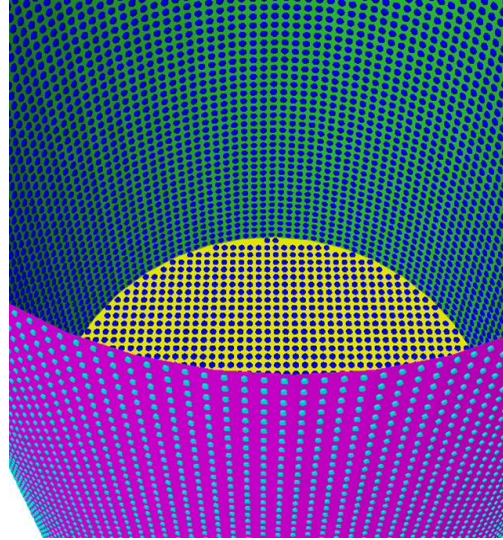


**Figure 1.20:** Output of RAYTRACER showing the OD wall and ID volume. The top caps of both the ID and OD were removed. The external PMTs (cyan) are on the OD wall (purple), and the inner PMTs (blue) are shown on the ID wall (green), and the ID bottom cap (yellow).

### Conclusions

RAYTRACER can now be used along with OGLSX in the WCSIM code, which will allow users to visualize any geometrical properties of simulated Water Cherenkov detector components. This is especially useful for Hyper-K, as the design is being finalized and simulations are being run to optimize its geometry. Using RAYTRACER as a visualizer, the outer detector was created and implemented in the WCSIM code. This will create more accurate simulations of the neutrino detectors. Future work on the design of the outer detector in WCSIM will consist of adjusting the outer detector PMT cap placement and creating a final outer wall in place around Super-K.

## 1.8 Estimating Detector Efficiency and Statistical Errors in HALO

D.S. RIGGIN, K. SCHOLBERG, *Duke University, Durham, NC*

Updates to the GEANT4 simulation of the Helium and Lead Observatory (HALO) have been made. We use the current simulation to get new single- and double-neutron tagging efficiencies and use them to calculate error contours for inferring “real” events numbers from data. By superimposing these contours on known single and double neutron interaction rates for different supernova models, we estimate that HALO will have reasonable physics sensitivity for supernovae up to 10 kpc away.

The Helium and Lead Observatory (HALO) is a dedicated supernova neutrino detector located at Sudbury Neutrino Observatory (SNO-LAB) in Sudbury, Ontario. HALO is made up of 79 tons of lead and 128  $^3\text{He}$  neutron-counter detectors (NCDs). It is sensitive to core-collapse supernovae and detects neutrinos through both charged- and neutral-current interactions. HALO is part of the SuperNova Early Warning System (SNEWS), a system intended to alert astrophysicists to the fact that a supernova has occurred. This summer, the Duke Neutrino Group repeated previous studies done on the physics sensitivity of HALO using the updated HALO GEANT4 simulation. The physics sensitivity of the detector is important for determining how much information we will be able to glean about supernovae from detection of their neutrinos in HALO.

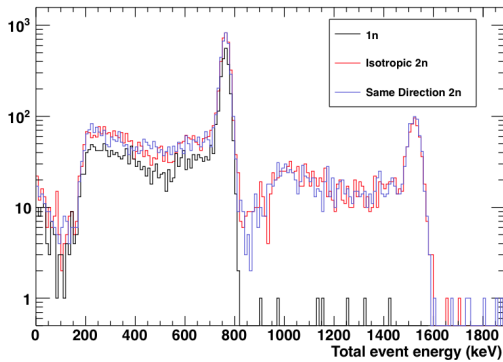


Figure 1.21: Energy spectrum of 1n and 2n helium-counter events in HALO [Sch11].

The first of our goals was to determine the neutron tagging efficiency for single- and double-

neutron (1n and 2n) events. To do this, we use methods developed by Schafer and Moss [Sch11] based on the energy spectra of these events in the  $^3\text{He}$  NCDs. Such a spectrum is shown in Fig. 1.21. The 1n events have a single peak in energy around 800 keV where all the energy from a single neutron is collected, whereas 2n events have a second peak in energy around 1600 keV where all the energy from both neutrons is collected. Using this information, we used a kinematics file-generator to run  $10^4$  of each of the following type of events: 1n and 2n events where the neutrons had initial kinetic energies of 0.5 MeV to 10.0 MeV, incrementing by steps of 0.5 MeV. Using the energy deposited in the  $^3\text{He}$  NCDs, we determined how many neutrons each event was tagged as containing and came up with the tagging efficiencies shown in Fig. 1.22.

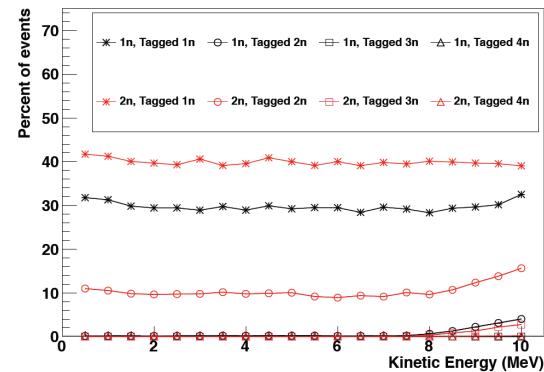


Figure 1.22: Neutron tagging efficiencies in HALO for neutrons with different kinetic energies from 0 to 10 MeV in steps of 0.5 MeV.

Next, we wanted to use these tagging efficiencies to create physics-sensitivity plots. We calculated matrices for neutron tagging efficiency us-

ing the equation

$$A(n) = \begin{pmatrix} 1n \text{ tagged } 1n & 2n \text{ tagged } 1n \\ 1n \text{ tagged } 2n & 2n \text{ tagged } 2n \end{pmatrix} \quad (1.16)$$

where  $n$  is the initial kinetic energy of the neutron. We then used these matrices and normalized the energy spectra for charged and neutral current interactions of neutrinos with lead calculated by Kolbe and Langanke [Kol01] to weight them and obtain the total tagging efficiency matrix across all considered neutron kinetic energies shown in Eq. (1.17).

$$B_{ij}(E_n) = \sum_{E_n} f(E_n) A_{ij}(E_n) \quad (1.17)$$

We picked three initial arbitrarily “true” points within different groups of supernova models from Väänänen and Volpe [Vää11]. Using toy-Monte-Carlo methods and Poisson random number generation, we fluctuated around these three points for more true events. Then, using the matrix calculated in Eq. (1.17), we inferred possible observed events from these true events and drew error contours that would enclose at least 90% of all the inferred points. Superimposing these plots onto the models of supernovae resulted in Fig. 1.23 for a supernova at 10 kpc and Fig. 1.24 for a supernova at 5 kpc from HALO.

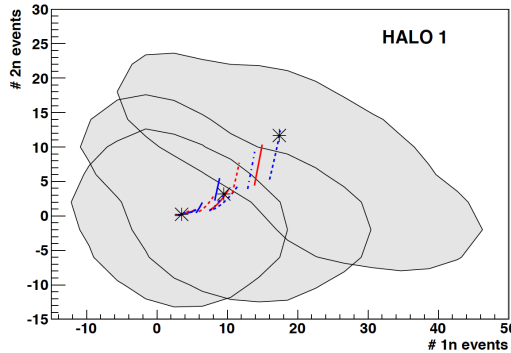


**Figure 1.23: Physics sensitivity in HALO for a supernova at 10 kpc. For any given true event, we will be able to rule out about half the models of supernovae it could represent.**

After making these calculations, we used the same methods to predict the physics sensitivity at 10 kpc for HALO 2, yielding the results shown in Fig. 1.25. HALO 2 is an idea for a new HALO that would be made with 1 kiloton of lead.

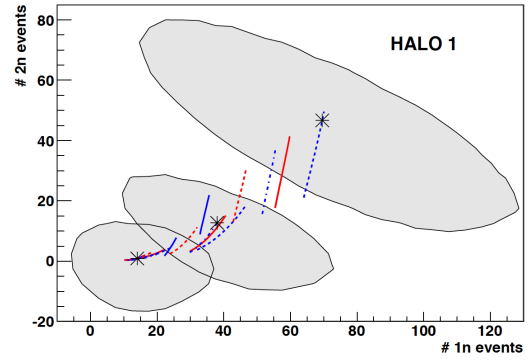


**Figure 1.24: Physics sensitivity in HALO for a supernova at 5 kpc. At 5 kpc many of the models can be ruled out for any given true number of events.**

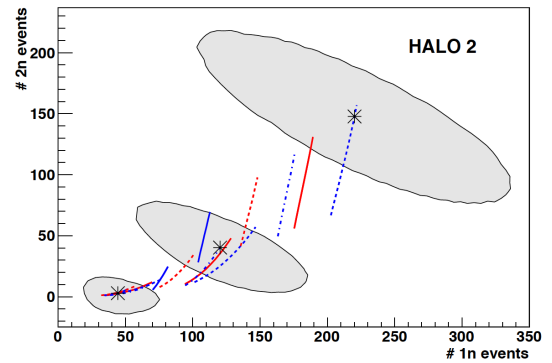


**Figure 1.25: Physics sensitivity prediction at 10 kpc for HALO 2, which will be built using 1 kiloton of lead.**

From these plots, we conclude that in the current HALO we could rule out about half the supernovae models if we are given a specific measurement for a supernova at 10 kpc, and many of the models for a supernova at 5 kpc. If HALO 2 is built, we will be able to rule out many models for a supernova at 10 kpc. Both detectors have reasonable predicted physics sensitivity and therefore could yield valuable information from their measurements of supernova.

[Kol01] E. Kolbe and K. Langanke, *Phys. Rev. C*, **63**, 025802 (2001).

[Sch11] L. Schaefer and A. Moss, *Study of 1n and 2n Production in HALO*, 2011, internal HALO document from Duke University.

[Vää11] D. Väänänen and C. Volpe, *J. Cosmol. Astropart. Phys.*, **2011**, 019 (2011).

# Research Based at CERN

---

Chapter 2

## 2.1 Searches for New Force Carriers with the ATLAS Experiment

O.M. AMRAM, A.T. GOSHAW, S. LI, A. BOCCI, *Duke University*

As part of the search for the predicted  $X$  boson, the focus of this project is to compare two different jet-analysis algorithms and determine their efficiencies for reconstructing  $X \rightarrow V\gamma$  events in the ATLAS detector, where  $V$  stands for a vector boson. It was found that the fat-jet algorithm could successfully reconstruct the vector boson in such events with approximately 70% efficiency, compared to a roughly 7% efficiency for the resolved-jet algorithm.

### Background

Many theories of physics beyond the standard model involve heavy scalar (spin-0) or vector (spin-1) particles. These new bosons would be carriers of new forces, beyond those of the standard model. Many of these theories predict new forces as a way to better understand electroweak symmetry-breaking, the process by which the force carriers of the electroweak force came to have mass. In Run-II of the Large Hadron Collider (LHC), the ATLAS collaboration will perform a model-independent search for such resonances decaying to  $V\gamma$ , where  $V$  is a vector boson (either a  $W$  or a  $Z$ ).

In Run II, the LHC will reach sufficient energies and luminosity for us to search for the predicted  $X$  boson. The LHC will operate at a center-of-mass energy of 13 TeV, which will allow for searches of massive, TeV-scale particles, with a precision not possible in Run-I. While no one knows what we will see when the analysis of Run-II data from the ATLAS experiment begins, there are small clues from the Run-I data. In Run-I, ATLAS found a small peak at 2 TeV for  $X \rightarrow VV'$ , where  $V$  stands for a vector boson (a  $W$  or  $Z$ ). While there were not enough data to be conclusive, these results lend excitement to the possibility of a new 2-TeV particle.

The two main advantages in looking for  $V\gamma$  final states instead of  $VV'$  final states are that:

- The high energy photon provides a clean trigger to select events of interest; and
- The acceptance range in  $\eta$  of photons in the ATLAS detector is nearly twice that of the jets produced by the decaying  $V$ .

In this study, the low-scale Technicolor model was used as a benchmark model to study the

$X \rightarrow V\gamma$  reaction, where the vector boson subsequently decays into two quarks  $V \rightarrow q\bar{q}$  (see Fig. 2.1). These sample events were generated with a mass of 2 TeV. The goal of such an analysis is to reconstruct the correct invariant mass for the  $X$  boson from the 4-vectors of the photon and  $q\bar{q}$ . Experimentally, the photon is measured well in the detector, and the quarks less so.

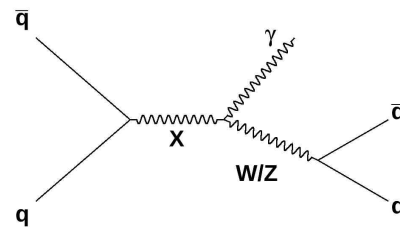


Figure 2.1: Feynman Diagram showing an  $X$  particle produced from a quark anti-quark pair and decaying by  $X \rightarrow V\gamma$  and the vector boson decaying into quarks.

### Jet Clustering

One of the major challenges in any analysis done at the LHC is trying to reconstruct the final-state quarks of a reaction. Due to confinement, free quarks can never exist. Thus when quarks are produced in a decay reaction, what actually reaches the detector is not the quarks themselves but a shower of particles, called a jet. The difficulty is in trying to reconstruct the original kinematics of the quarks from these showers.

The most basic question is to decide which particles should be assigned to which jets. To do this we define a cone in  $\Delta R$ , which is essentially a measure of angular distance defined by  $\Delta R^2 = \Delta\eta^2 + \Delta\phi^2$ , where  $\eta$  is pseudo-rapidity and  $\phi$  is the usual azimuthal angle.

There are two different jet-clustering methodologies that are possibly appropriate for this analysis. One is a resolved-jets approach (AntiKt4 jets), where the radius of the cone is small ( $\Delta R = 0.4$ ). It attempts to isolate each final-state quark in its own jet. This algorithm performs best when the quarks are well separated ( $\Delta R > 0.8$ ), so the particles from each shower are in separate cones. The other methodology is to use a fat-jet approach (AntiKt10 jets), where the radius of the cone is large ( $\Delta R = 1.0$ ). This model attempts to capture both quarks into a single large jet. It performs best when the quarks are close together ( $\Delta R < 0.8$ ), because then all of the particles from both showers can fit in the fat jet.

One goal was to determine which of these methodologies is appropriate for this analysis and to estimate their efficiencies at reconstructing the correct mass of the vector boson whose decay produced the quarks.

## Results

The results of our investigation are shown in Fig. 2.2. It was found that the distribution in  $\Delta R$  between the two final-state quarks was very narrow. This is due to the high energy of the produced  $W$  or  $Z$  boson, which is a result of the extremely high mass of the  $X$  particle. Because the vector boson is so energetic, its rest frame has a large Lorentz boost compared to the laboratory frame. This causes the angle between the two quarks in the laboratory to be very narrow.

This narrow distribution of  $\Delta R$  means that more than 90% of the time the two quarks fall within the  $\Delta R < 0.8$  range, which is ideal for the fat-jet approach. There is a sharp cutoff on the low end of the distribution, with no events having  $\Delta R < 0.2$ . This is a result of the model used to generate the events in the simulation and is not necessarily what we expect to see in real data.

Because of the narrow distribution in  $\Delta R$ , the fat-jet algorithms perform much better than the resolved-jet algorithms. One way to compare the effectiveness of the two approaches is to see the efficiency you find when you use the produced jets to reconstruct the correct mass of the vector

boson which produced them. With the fat-jet approach, we were able to successfully reconstruct the vector boson's invariant mass with a 70% efficiency. In comparison, with the resolved-jet approach, we were able to successfully reconstruct the vector boson's invariant mass with only about 7% efficiency.

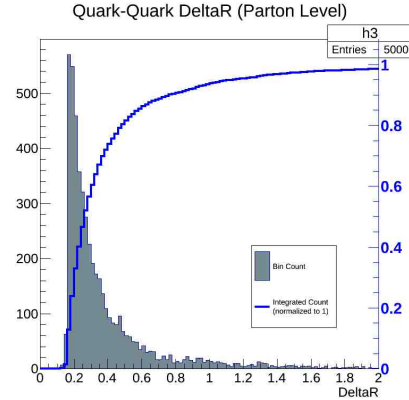


**Figure 2.2:** Distribution of  $\Delta R$  between the two quarks produced from  $V \rightarrow q\bar{q}$ . The dark blue line shows the percentage of events less than a given  $\Delta R$ . The narrow width of this distribution makes the fat-jet approach ideal.

While clearly the fat-jet approach performed an order of magnitude better than the resolved-jet approach, there is still room for improvement. When reconstructing the complete invariant mass of the  $X$  particle, the object of our search, there is a low-mass tail when using the fat-jet approach. This tail does not disappear when selecting for events where we successfully reconstructed the vector boson. Instead, the tail is due to the extra steps, called 'trimming,' that must be taken in using such a large cone for a jet. Trimming removes extra particles that are present in the cone but did not come from the initial quarks. It seems that in this case there is some over-trimming, or removing particles which should not be removed, creating this low mass tail.

It is also worth pursuing the possibility of using resolved jets in certain kinematic regions, in some sort of hybrid approach, in order to improve upon the overall efficiency.

---

## 2.2 Visualization Studies for Advanced Jet-Tagging Algorithms

---

D.J. ELOFSON, A.T. ARCE, M. EPLAND, *TUNL*;

**Jet-tagging algorithms analyze lists of data from high-energy particle collisions to define the jets of particles produced in the interaction, but little is known about how they work and why they have the outputs they do. We have created a program in ROOT that generates multiple visualizations of jets, including one that displays a two-dimensional histogram showing how each individual algorithm operates on a set of data. This reveals why each algorithm gives a different output based on the way it operates on the dataset.**

When two particles collide at a high energy, new particles may be created. They will then decay into quarks with extremely high kinetic energies. At some point the magnitude of the strong force caused by the distance separating the quarks is large enough that hadronization occurs to preserve color neutrality. These new particles can also decay and the process continues until the products pass into the detector and the process is stopped. This phenomenon, where one particle creates a final end product of many particles with similar transverse momenta  $p_t$  is called a jet.

Studying these jets is extremely useful when trying to determine the original particles that were created from the collision. Unfortunately, defining and illustrating the jets is difficult, because there is no truly correct way to go about determining which particle is part of which jet, and the amount of information needed from a jet is always hard to fit into a single picture.

When two particles collide in ATLAS, the data are given in a table where each row represents a particle and each column is a property of that particle including  $p_t$ ,  $\eta$ ,  $\phi$  and  $E$ . Each collision can involve hundreds of particles, and the first goal when analyzing the data is to separate these particles into their respective jets. This would be easy to do if a jet were defined as a radius around the most energetic particle, but all of the jet algorithms show that it is not that simple.

Jet algorithms come in many varieties. The first large group are called cone algorithms and involve the assumption that a jet will be in the shape of a cone with a given cross section in the rapidity- $\phi$  plane. The cone algorithms differ in the way they deal with the issue of overlapping cones. These algorithms include the itera-

tive cone algorithm with progressive removal (IC-PR), fixed cone with progressive removal (FC-PR), the split-merge (IC-SM) and split-drop (IC-SD).

Each new algorithm was created in order to improve the effectiveness of its predecessor by improving the infrared and collinear (IRC) safety. This property tells whether or not the output of the jet algorithm will be the same based on minute changes in the final particles. For instance, theoretically a jet is supposed to be all of the final particles that were created and emitted from a larger original particle. As the particles split into quarks and hadronize, each new particle should be contained in the same jets as the original particles that created them. If, for example, the most energetic particle in a jet splits into two less energetic, basically collinear particles and the algorithm gives a different set of final jets, the algorithm is collinear unsafe. On the other hand, if the emission of a gluon causes a different output from the algorithm, it is considered infrared unsafe.

The search for IRC safety has led to the second larger group called sequential recombination algorithms. Included in these are the  $k_t$ , Cambridge-Aachen and anti- $k_t$  algorithms. Although all different, they each come from the same set of equations.

$$d_{ij} = \min(p_{ti}^{2p}, p_{tj}^{2p}) \frac{\Delta R_{ij}^2}{R^2} \quad (2.1)$$

$$\Delta R_{ij}^2 = (y_i - y_j)^2 + (\phi_i - \phi_j)^2 \quad (2.2)$$

$$d_{iB} = p_{ti}^{2p} \quad (2.3)$$

The only difference in the algorithms is the value of  $2p$ , the exponent of  $p_t$ . The  $k_t$  algorithm uses softer (lower  $p_t$ ) particles to build jets and

therefore uses a value of  $p = 1$  and the anti- $k_t$  algorithm favors harder (higher  $p_t$ ) particles, so it uses a value of  $p = -1$ . The Cambridge/Aachen algorithm is different because it operates independently of energy and therefore uses a value of  $p = 0$ .

Duke uses a program called FASTJET, which allows use of both Cambridge/Aachen and anti- $k_t$  to define jets. As mentioned earlier, it is hard to show all the important information in a single illustration or event display. To find the most effective way to display this information, a survey was distributed, asking people to rate six different event displays based on ease of interpretation and visual appeal. The cylindrical CMS display was rated highest, with the black-and-white CMS lego event display rated second highest. To accommodate this input, the new program has incorporated lines to display data in both a lego plot and a cylindrical pseudorapidity lego plot.

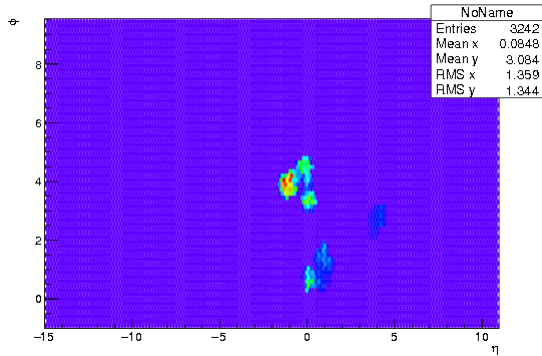


**Figure 2.3:** Ghost plot of data using the Cambridge/Aachen algorithm with  $R = 1.0$  on the  $\eta$ - $\phi$  plane. Red particles are found first while blue particles are found last.

The lego plot works by giving a weight to each particle filled into the histogram according to its  $p_t$ . Both plots are from the same data set and only show the three hardest jets, so as to keep the plots simple.

The next step involved adding ghost particles with  $p_t = 1e - 50$  to the data in order to define the jet area. When this is done, it is

easy to see how the jet algorithms differ. The anti- $k_t$  algorithm gives very circular jets, whereas the Cambridge/Aachen algorithm gives irregularly shaped jets. This is due to the fact that the Cambridge/Aachen does not depend on energy and therefore gives the same consideration to the ghosts as it does to the actual particles, whereas the anti- $k_t$  focuses on the harder particles and therefore gives a circular jet arranged around the central, highest  $p_t$  particle.

In order to determine how the algorithms work, a weight was given to the ghosts based on the order they were found and recorded by the program. The ghosts were then filled into a TH2Poly histogram, colored by weight to produce Figs. 2.3 and 2.4.

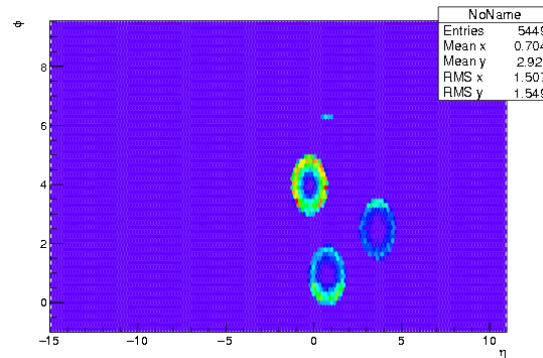


**Figure 2.4:** Ghost plot of the same data using the anti- $k_t$  algorithm with  $R = 1.0$  on the  $\eta$ - $\phi$  plane. Red particles are found first while blue particles are found last.

It is important to note that the ghost plot of the anti- $k_t$  algorithm output shows that the algorithm finds ghosts on the outside of the jet and works its way in. This suggests and confirms that it works by finding the hardest particle and creating a jet around it before filling in the rest of the area. The ghost plot of the Cambridge/Aachen algorithm output shows that there is no specific direction or centering around any particular particle. This goes along with the knowledge that the algorithm works only by angular distance and not by energy.

## 2.3 Upgrades and Development for the Semiconductor Tracker of the ATLAS Detector

A. SMITH, A. ARCE, S. BURANT, M. KRUSE, C. LINDEMAN, M. TOBIN, C. ZHOU, *Duke University*

The Semiconductor Tracker of the ATLAS detector will undergo complete replacement before Phase II operation of the Large Hadron Collider commences in the early 2020s. To protect the new tracker electronics we constructed a prototype interlock system to monitor temperature and humidity. At CERN, we recommissioned the single module test system. Our tests indicate that system noise decreases as more voltage is applied to the semiconducting sensor, validating previous hardware studies.

### Introduction

The Large Hadron Collider (LHC) at the European Organization for Nuclear Research (CERN) in Geneva, Switzerland, has just begun Run 2 of proton-proton collisions after sustaining a scheduled shutdown since 2012. Beginning in Run 2, collisions will occur every 25 ns at an increased center of mass energy of 13 TeV. From approximately 2025 onward, the LHC experiments aim to accumulate data corresponding to an integrated luminosity (number of events per unit cross section) of  $3000 \text{ fb}^{-1}$ . To meet the demands of higher luminosities, one of the principal detectors, A Toroidal LHC Apparatus (ATLAS), will undergo a series of upgrades to the electronics and infrastructure of the inner Semiconductor Tracker (SCT).

When two proton beams cross in the detector, a host of interactions and decays generates new particles which interact with the different trackers, calorimeters, and muon chamber of ATLAS. The SCT is specifically designed to track the momentum of charged particles within  $|\eta| < 2.5$ , as they curve under the 2-tesla magnetic field permeating the inner detector [Arg14]. Here  $\eta$  is the pseudorapidity.

In the ultimate electronics design, a ten-chip column is wire-bonded onto a board to form a hybrid. The hybrid is then glued to a silicon sensor comprised of 2560 channels—256 channels per chip—to form a module. Several modules attach linearly to form stavelets, and stavelets are further connected to form staves. The new SCT barrel will be comprised of five layers of staves, and the SCT endcaps will feature similar electronics configured in a petal design [Gre14].

The upgrades to the SCT design have sev-

eral motivations. First, higher luminosities at the future LHC demand better channel resolution to mitigate the effects of pile-up at each bunch crossing. Second, the decreased chip size from 250 nm to 130 nm will make the electronics more radiation-hard.

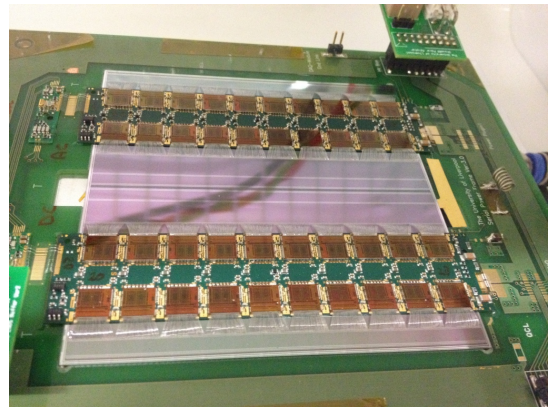


Figure 2.5: The intermediate design of a single module with which we worked. The final design will have one column of chips per hybrid, not two as pictured.

### Devising an Interlock

Duke University currently has a single-chip test stand and, in anticipation of receiving an entire single module, is spearheading designs for testing a module system. Our task was to design and implement a temperature- and humidity-controlled environment to house the future single module. To ensure the electronics do not overheat, a cooling line capable of  $-40^\circ \text{C}$  will be run under the module. However, cooling below the dew point introduces the danger of condensation. To account for the dual threats, we designed an interlock system which shuts off power to the module

if temperature or humidity goes out of range.

To implement these environmental controls, a de-localized SparkFun sensor is placed near the chips and sends temperature and humidity data to an Arduino board. If danger thresholds are exceeded, a current pulse is sent to the Printed Circuit Board (PCB). The pulse converts to a voltage drop by passing through an LED, triggering the innate interlock of the module’s power supply.

### Testing a Single Module

The single module equipment at CERN underwent a nontrivial relocation from Building 180 to a new testing facility at SR1. Following the move, we reconnected the power supplies, electronics, and computers to ensure that the SCT data acquisition system was communicating correctly with the single module and that all hardware was fully functional. We were assigned the task of characterizing the noise levels of the setup, particularly as a function of the high voltage bias applied to the silicon sensor. Applying voltage widens the depletion region of the sensor, in theory increasing efficiency in the generation of current as a charged particle passes through.

To obtain the plot in Fig. 2.6, we performed a Three-Point Gain scan. The scan injects three charge levels of 0.52, 1.00, and 1.48  $fC$  and calculates the spread in thresholds detected by the chips at the given charge [Arg12]. The spread, measured in mV, is divided by the gain and converted to equivalent-noise charge (ENC). The vertical axis of the plot reports noise in units of ENC.

In the single module we tested, the four columns of chips—here denoted as “streams”—responded as expected. Our tests show that the higher sensor biases result in less system noise, and thus increased tracking efficiency. There appears to be a limit to the advantage of sensor biasing, however, and the stream noise tapers more slowly past 175 V. We also recorded noise values for an unbiased sensor at 0 V. Those mean noise values well exceeded 3000 ENC and are therefore excluded from the plot.

We conclude from these results that the high voltage supply is interfacing as expected with the module. The plateau effect we observe may be linked to the increased leakage current of the sensor at higher biases, perhaps counteracting greater efficiencies. We could not exceed the 250 V upper limit of our tests due to concerns of exceeding 100  $\mu A$  of leakage current.

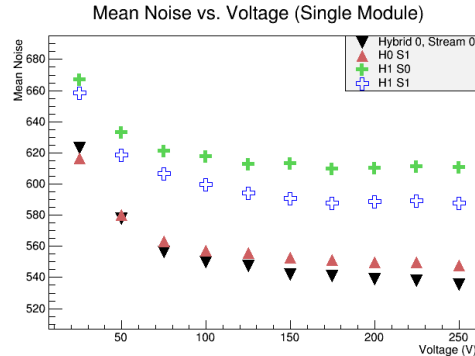


**Figure 2.6:** The mean noise versus the high voltage sensor bias, obtained from the Three-Point Gain scan. Note the apparent plateau in noise beyond 175 V.

Ultimately, our work on these projects has led to better documentation both at Duke and CERN regarding the single module system. The infrastructure advances will also pioneer optimal setups for future collaborators seeking to build their own test stands. Future steps in the SCT upgrade include transitioning from the current High Speed Input Output (HSIO) board to the more cost-effective, scalable Atlys board and establishing operations with the stavelets in SR1.

[Arg12] C. G. Argos, *Procedure for operating the HSIO DAQ system for single modules in the B180 setup*, ATLAS internal document, 2012.

[Arg14] C. G. Argos, Ph.D. thesis, Valencia University, 2014.

[Gre14] I.-M. Gregor, *Overview, ATLAS ITK Strip Detector*, Technical report, DESY, 2014.

---

## 2.4 R & D for the ATLAS Semiconductor Tracker Upgrade

---

C. LINDEMAN, A. ARCE, S. BURANT, M. KRUSE, A. SMITH, M. TOBIN, C. ZHOU *Duke University*

**The current Semiconductor Tracker in the ATLAS detector at CERN will be replaced as part of a larger detector upgrade. Working at Duke University, we designed a temperature and humidity interlock system to protect the electronics. Then at CERN, we commissioned the data acquisition systems for silicon detector components and ran noise tests at several temperatures. As expected, we found that lower temperature corresponds to lower noise levels and thus more suitable conditions for taking data.**

### Introduction

At approximately 27 kilometers in diameter, the Large Hadron Collider (LHC) at the European Organization for Nuclear Research (CERN) is the largest particle collider in the world. The current electronics and detectors are designed for proton-proton collisions at 14 TeV in the center-of-mass frame [Fel02]. However, scientists at CERN hope to probe even further and have planned a series of upgrades to the various detectors. Among these is an upgrade to A Toroidal LHC Apparatus (ATLAS) scheduled to occur around 2026. In particular, the innermost detector of ATLAS will be replaced by an all-silicon detector [Van11].

There are two major reasons for this upgrade. First of all, by 2026, the inner detector will have received such a large radiation dose that it will no longer be able to perform at the level needed. Moreover, as the beam luminosity is increased, the number of pile-up events will exceed the current capacity [Van11].

Among the changes being made to the inner detector are major revisions to the basic design of the Semiconductor Tracker (SCT). As in the current SCT, the new designs center around silicon strips that are ionized when a charged particle passes through, sending an electronic pulse to the readout electronics. In the new design, 2560 such strips, called channels, are grouped together in a module, which in turn is grouped with other modules to form a stavelet. Finally, the stavelets are set end-to-end to create a stave, which acts as one slat in the cylinder shape surrounding the collision point. Farther along the beamline, modules are grouped instead into petalets, which are situated normal to the beamline to detect higher- $\eta$  particles, where  $\eta$  is the pseudorapidity.

There are two parts to the research described in this paper. The first explains work done developing a temperature interlock system at Duke University, which is in the process of preparing to receive a module for testing. The second goes over a series of noise tests run on a module currently situated at CERN.

### Duke University Interlock System

Although Duke currently has only a single chip and its associated 128 channels, it will soon receive an entire 2560-channel module and is in the process of designing a system to accommodate it. In addition to an environment free from ambient dust particles and moisture, the chip needs an interlock system.

The main concerns in keeping a module and all the associated channels free from damage are heat and moisture. For this reason, it is critical to have some sort of interlock system that will cut off power to the chips if either the temperature or the humidity exceed a threshold level. Certain power supplies help facilitate this safety feature by shutting themselves off if the voltage goes above a specified level.

We designed and ordered a printed circuit board (PCB) that will ultimately connect with such a power supply. The PCB, shown in Fig. 2.7, makes use of an Arduino board to generate a current whenever the temperature or humidity, as measured by a SparkFun monitor, goes over the set value. The PCB activates an LED and converts this current to a voltage drop so that the pulse can be read out to the power supply, stopping the current and preventing damage to the chip.

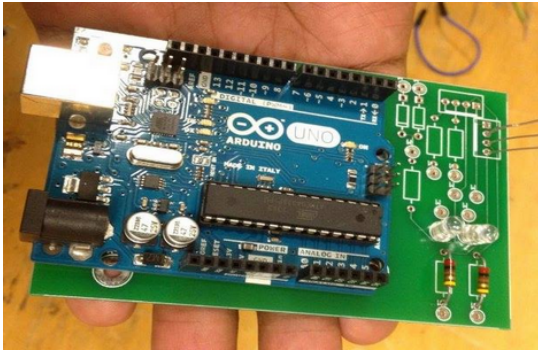


Figure 2.7: The printed circuit board with some components soldered on and the associated Arduino board attached.

### CERN Module Testing

The module at CERN is already protected by a temperature interlock system developed by Cambridge University. However, the entire module set-up was recently relocated from Building 180 to SR1, another clean room. After reconnecting everything, our role in testing the module was to ensure that it still behaved as expected and, in particular, that the noise levels were similar to those before the move.

We relied primarily on a program called a Three Point Gain scan, which injects three different charges (0.52, 1.0, and 1.48 fC) and reads out the variance of the threshold distribution for each charge. This output is considered the noise, and is measured in mV [Arg12].

One expected feature of such noise for a semiconductor is that it will increase as a function of temperature. To test this, we set the chiller to various temperatures and ran a Three Point Gain scan at each. In addition to the average noise for each 10-chip (1280-channel) stream, we also recorded the actual temperature of the module during the test. The values set on the chiller and the measured values recorded are both shown in table 2.4.

Table 2.1: Chiller temperature set and module temperature read out for each scan run.

Set ( $^{\circ}\text{C}$ )	6	9	12	15	18
Read ( $^{\circ}\text{C}$ )	19	22	25	27	30

There were two chips that were continually problematic during general testing, and we came to the conclusion that they likely have wirebonding issues and should not be included in these noise tests. These two chips were thus disabled and their collective 256 channels were not included in the averages.

Figure 2.8 shows the noise for each of the four streams as a function of the measured temperature. Note that the points corresponding to all four streams indeed increase as the measured temperature increases, indicating agreement with the expected behavior.

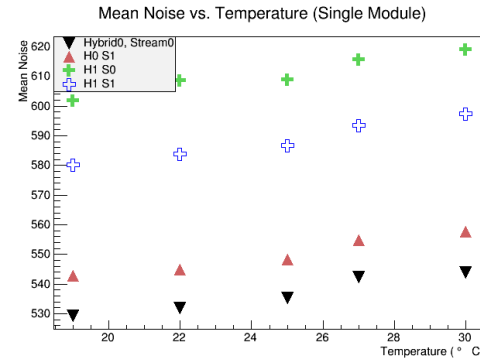


Figure 2.8: The average noise per stream vs the module temperature during the Three Point Gain scan. Each of the four streams is read out separately.

In particular, each stream seems to follow a fairly linear trend, which matches the results of Three Point Gain scans run in Building 180, before the relocation of the equipment [Arg14]. We thus conclude that, aside from the two previously-mentioned chips, the module remains in good working condition.

Now that the module has been tested and is confirmed to be working as expected, there are two major goals for future work. First, steps can be made toward getting the stavelet located at CERN connected and tested. In addition, the High Speed Input/Output (HSIO) board used by the module will eventually need to be replaced by an Atlys board, a commercial and relatively inexpensive alternative to the custom-made HSIO board.

[Arg12] C. G. Argos, *Procedure for operating the HSIO DAQ system for single modules in the B180 setup*, ATLAS internal document, 2012.

[Arg14] C. G. Argos, Ph.D. thesis, Universidad de Valencia, 2014.

[Fel02] L. Feld, Nucl. Instrum. Methods A, **478**, 277 (2002).

[Van11] P. Vankov, In G. Bernardi, S. D. Cecco, and Y. Enari, editors, *Proceedings of the Hadron Collider Physics Symposium*, 2011.

# Index

(Listed by corresponding author)

Amram, O.M., 19

Bray, I., 2

Elofson, D.J., 21

Kowal, K.M., 4

Lindeman, C., 25

Masood, K., 6

Niazi, R., 8

Nibbs, K., 10

Olmsted, S.C., 12

Perreau, N., 14

Riggin, D.S., 16

Smith, A., 23